



AIAA 2001-3199

**Transonic Investigation of
Two-Dimensional Nozzles
Designed for Supersonic Cruise**

F. J. Capone and K. A. Deere
NASA Langley Research Center
Hampton, Virginia

**37th AIAA/ASME/SAE/ASEE
Joint Propulsion Conference and Exhibit
8-11 July 2001
Salt Lake City, Utah**

Transonic Investigation of Two-Dimensional Nozzles Designed for Supersonic Cruise Aircraft

Francis J. Capone[†] and Karen A. Deere^{*}

Aerodynamics, Aerothermodynamics and Acoustics Competency
NASA Langley Research Center, Hampton, Virginia

ABSTRACT

An experimental and computational investigation has been conducted to determine the off-design uninstalled drag characteristics of a two-dimensional convergent-divergent nozzle designed for a supersonic cruise civil transport. The main objective of this investigation was to determine the effects of varying nozzle external flap curvature and sidewall boattail angle and curvature on nozzle drag. The experimental investigation was conducted in the Langley 16-Foot Transonic Tunnel at Mach numbers from 0.80 to 1.20 at nozzle pressure ratios up to 9. Three-dimensional simulations of nozzle performance were obtained with the computational fluid dynamics code PAB using turbulence closure and nonlinear Reynolds stress modeling. The results of this investigation indicate that excellent correlation between experimental and predicted results was obtained for the nozzle with a moderate amount of boattail curvature. The nozzle with an external flap having a sharp shoulder (no curvature) had the lowest nozzle pressure drag. At a Mach number of 1.2, sidewall pressure drag doubled as sidewall boattail angle was increased from 4° to 8°. Reducing the height of the sidewall caused large decreases in both the sidewall and flap pressure drags.

INTRODUCTION

The National Aeronautics and Space Administration sponsored a joint High-Speed Research Program with US airframe and propulsion companies to provide the critical high-risk technologies for a Mach 2.4, 300 passenger aircraft (ref. 1). One task the NASA-industry team faced was what type of exhaust nozzle would be best for the High Speed Civil Transport propulsion system. The technical challenges addressed as part of the task involved developing a low-noise nozzle with high aerodynamic efficiency, low weight and long life. Trade studies indicated that a two-dimensional convergent-divergent nozzle would be best suited to meet the very stringent noise requirements of the HSR program.

The engine cycle chosen for the HSCT propulsion system was a mixed-flow turbofan.

Although this cycle did have a moderate bypass ratio, a mixer-ejector type nozzle would be necessary to reduce engine noise. One of the nozzle concepts considered is shown in figure 1. An ejector would entrain outside free stream air at take-off conditions through bypass doors integrated with the nozzle. During transonic and supersonic cruise conditions, these doors would be closed since external air entrainment would not be necessary.

A major problem in designing an exhaust system for a supersonic cruise vehicle is that its geometric shape must change as flight conditions vary. The nozzle exit area ratio has to be varied continuously to maintain high performance at all flight conditions from takeoff to supersonic cruise. Nozzle performance cannot be comprised at supersonic conditions since payload weight is highly sensitive to nozzle efficiency. For example, a 1-percent decrease in nozzle performance has been estimated to be equivalent to about an 8-percent loss in payload for this class of aircraft (ref. 2).

The nozzle operates with the largest area ratio at supersonic cruise. In order to reduce flow angularity losses (flow not exiting parallel to nozzle center line), the divergent flap half-angle and thus, length, are set to provide maximum internal performance at the supersonic design point for a fully expanded area ratio. As seen in the schematic in figure 1, the nozzle would have very long divergent flaps. At subsonic cruise, the nozzle would operate at a much lower area ratio.

[†]Senior Research Engineer,
Configuration Aerodynamics Branch

^{*}Aerospace Engineer,
Configuration Aerodynamics Branch, Member
AIAA

Copyright © 2001 by the American Institute of Aeronautics and Astronautics, Inc. No copyright is asserted in the United States under Title 17, U.S. Code. The U. S. Government has a royalty-free license to exercise all rights under the copyright claimed herein for government purposes. All other rights are reserved by the copyright owner.

Consequently, long external flaps are required to minimize the nozzle boattail angle and resultant nozzle boattail drag. Another factor that can influence boattail drag is the curvature at the start of the boattail.

The nozzle boattail drag can be a significant part of the overall drag at subsonic speeds. Several studies were also conducted that addressed installed nozzle boattail drag issues. These studies suggested that nozzle boattail drag could be as much as 25 to 40 percent of the subsonic cruise drag (ref. 3) for the HSCT aircraft. Since limited experimental data exists for this class of nozzles, an experimental and computational program was initiated at NASA-Langley to determine the uninstalled drag characteristics of this nozzle concept. The overall objectives were to: (1) determine the effects of nozzle external flap curvature and sidewall boattail variations; (2) develop an experimental data base for 2D nozzles with long divergent flaps and low boattail angles and (3) provide data for correlating CFD predictions of nozzle boattail drag.

The experimental investigation was conducted in the Langley 16-Foot Transonic Tunnel at Mach numbers from 0.80 to 1.20 at nozzle pressure ratios up to 9. Three-dimensional simulations of nozzle performance were obtained with the computational fluid dynamics code PAB using turbulence closure and nonlinear Reynolds stress modeling.

SYMBOLS AND ABBREVIATIONS

$C_{D,f}$	nozzle friction drag coefficient
$C_{D,n}$	nozzle drag coefficient
$C_{D,p}$	nozzle pressure drag coefficient
$C_{D,p,f}$	flap pressure drag coefficient
$C_{D,p,s}$	sidewall pressure drag coefficient
$C_{p,f}$	flap pressure coefficient
$C_{p,s}$	sidewall pressure coefficient
CFD	computational fluid dynamics
EXP	experimental
F	flap
h_m	height of nozzle, in.
HSCT	high-speed civil transport

L_f	length of flap, in.
L_s	length of sidewall flap, in.
M	free-stream Mach number
MS	model station, in.
N	nozzle
NPR	nozzle pressure ratio
r_f	flap radius of curvature, in
r_s	sidewall radius of curvature, in
S	sidewall
β_f	flap boattail angle, deg
β_s	sidewall boattail angle, deg

NOZZLE DESIGNS

Overall Nozzle Geometry. The overall nozzle geometry is shown in figure 2. For the experimental portion of this study, the nozzle was sized to be tested on an existing propulsion simulation system in the Langley 16-Foot Transonic Tunnel. Thus the nozzle had a maximum height of 6.20 inches, a maximum width of 6.80 inches and an aspect ratio of 1.10 (width to height). However, some of the full-scale nozzle concepts being considered for the HSCT vehicle like that shown in figure 1, had aspect ratios of 1.04. Because of this difference in nozzle aspect ratio, the height of the nozzle was chosen for scaling purposes, since this parameter should give the best representation of nozzle boattail closure. This resulted in the model scale being 8.2-percent. From this scale, an appropriate reference area can be obtained for subsequent use in nondimensionalizing drag in order to produce meaningful drag coefficients in terms of airplane drag counts.

All nozzles tested had the same internal geometry, because only external nozzle geometry parameters were varied. The nozzles had a throat height h_t of 2.02 inches, an exit height h_e of 2.70 inches and an area ratio A_e/A_t of 1.34 (fig. 2). The corresponding nozzle design pressure ratio was 5.0. Thus changes in performance should only be attributed to external flow effects over the nozzle flaps. The overall length of the nozzle was 13.14 inches.

All nozzles were tested with sidewalls. The height of the sidewall was fixed to a distance

such that the nozzle internal flaps would not unport with the nozzle in the supersonic cruise position. In this position the boattail angle of the external flaps would be less than 4° . The sidewall cross sectional shape and maximum thickness were dictated from structural and actuation requirements for the full-scale nozzle.

External Flap and Sidewall Geometry.

The parameters used to define the nozzle external flap shape are shown in figure 3. Nozzle external flap length L_f and flap radius of curvature r_f were the two geometric parameters that varied during the test. These two parameters were nondimensionalized by the nozzle height h_m and maximum radius of curvature $r_{f,max}$. The baseline nozzle had a flap length of 8.42 inches. A shorter flap length of 6.74 inches was also tested. Note that the overall length of the nozzle, which is representative of the full-scale nozzle, was not changed when nozzle flap length was varied. Nozzles with boattail curvature parameters $r_f/r_{f,max}$ from 0 to 1 were tested. A nozzle with no curvature would probably be the simplest to build since this flap would have a simple hinge joint. If curvature were required, some type of a sliding mechanism at the hinge joint (fig. 1) would be necessary. The term $L_{a,f}$ represents the portion of the nozzle flap that is a circular arc. Nozzle flap F1 was considered the baseline flap for this investigation. Pretest predictions indicated that a nozzle with this flap would have the lowest drag.

The various parameters used to define the sidewall external shape are shown in figure 4. Sidewall boattail angle β_s and radius of curvature r_s were the two geometric parameters that varied during the test. Sidewall S1 was considered the baseline sidewall for this investigation.

Nozzle Configurations Tested. Nozzle configurations in which the external flap geometry was varied are presented in figure 5. The flap radius of curvature parameter was varied from 0 to 1.0 for nozzles N1, N2, N3, and N4 with the baseline flap length being held constant. Boattail angle varied from 11.72° to 23.44° for these configurations. Flap radius of curvature was also varied for the nozzles with the shorter flap length as indicated by nozzles N13 and N14. All these nozzles were tested with sidewall S1. Some tests were conducted with a reduced height sidewall with flaps F1

and F2 to determine whether a drag penalty may occur for the full height sidewalls.

The effect of varying sidewall boattail angle and radius of curvature were investigated for those nozzle configurations shown in figure 6. Sidewall boattail angle was varied from 4° to 8° for nozzles N1, N5 and N6 with $r_s/r_{s,max} = 0$. The sidewall radius of curvature parameter $r_s/r_{s,max}$ was varied from 0 to 0.4 for nozzles N5, N8, and N9 with the boattail angle at 6° and from 0 to 1.0 for nozzles N6, N6, and N10 with the boattail angle at 8° .

EXPERIMENTAL PROCEDURES

Wind Tunnel and Tests

This investigation was conducted in the NASA-Langley 16 Foot Transonic Tunnel which is a single-return, continuous-flow, atmospheric wind tunnel with a slotted octagonal test section and air exchange. The wind tunnel has a variable airspeed up to a Mach number of 1.25. A complete description of this facility and operating characteristics can be found in reference 4.

This investigation was conducted at Mach numbers from 0.80 to 1.20. Nozzle pressure ratio was varied from jet-off up to 9 depending on Mach number. Angle of attack was held at 0° . Reynolds number per foot varied from 3.8×10^6 to 4.2×10^6 .

Air Simulation System, Instrumentation

The nozzles were tested on an isolated, two-dimensional propulsion air-powered simulation system that was mounted in the wind tunnel by a sting/strut support system as shown in figure 7. A photograph showing this installation is presented in figure 8. The propulsion system is composed of three major sections: a nose-forebody, a centerbody section, and the nozzle. The nose-forebody section up to station 26.50 was nonmetric, that is, was not attached to the strain-gauge balance. The centerbody section was made up of the low-pressure plenum, instrumentation section and transition section. The centerbody section from station 26.50 to 50.90 was essentially rectangular in cross-section and had a constant width and height of 6.80 in. and 6.20 in. respectively. All nozzles connected to the centerbody section at model station 50.90. The metric portion of the model aft of model station 26.50, which was supported by the

force balance, consisted of the propulsion system, centerbody and nozzle. This simulation system is equipped with a flow transfer system that is designed to minimize the transfer of axial momentum across the force balance. An external high-pressure air system provided a continuous source of clean dry air to the model. A complete description of this propulsion simulation system can be found in reference 5.

An internal, six-component strain-gauge balance measured external aerodynamic forces and moments on the model downstream of model station 26.50. Mass-flow of the high-pressure air supplied to the nozzle was determined by a critical-flow venturi system located in the air lines external to the wind tunnel. Jet total pressure was measured in the instrumentation section by means of a 10-probe rake. A thermocouple, also located in the instrumentation section was used to measure jet total temperature.

The nozzle upper and lower flaps were each instrumented with two rows of pressure taps with 25 taps per row. On the upper flap, one row was located on the flap centerline and the other was located outboard near the sidewall. On the lower flap, one row was also located on the flap centerline and the other was located midway between the flap centerline and the outer edge of the flap. One of the nozzle sidewalls was instrumented with two rows of pressure taps with 20 taps per row.

Data Reduction

All data for both the model and the wind tunnel were recorded simultaneously on the facility computer disc. Fifty frames of data, taken at the rate of 10 samples/sec for 5 seconds, were used for each data point. Average values of the recorded data were used to compute standard force and moment coefficients. An appropriately scaled reference area for a HSCT transport was used to nondimensionalize drag in order to produce a meaningful drag coefficient in terms of airplane drag counts.

Force Measurements. The balance force measurements are corrected for model weight tares, balance interactions and flow transfer system (bellows) momentum tares. Although the bellows was designed to eliminate pressure and momentum effects on the balance readings, small bellows tares on all balance components still exist. These bellows tares were determined by testing calibration nozzles with known performance over a range of nozzle pressure ratios with balance loadings simulating

the ranges expected for the test nozzles. The balance data were then corrected in a manner similar to that discussed in references 5 and 6.

At wind-on conditions, the force balance measures all external and internal forces on the model downstream of model station 26.50. Included are nozzle thrust, nozzle drag (friction and pressure drag), centerbody friction drag (pressure drag equal to zero since the centerbody has no projected area), an axial force resulting from a pressure-area term acting at the metric break and the bellows momentum term.

Thrust minus nozzle drag was obtained by correcting the measured axial force to account for the various forces discussed above. Nozzle drag was then determined by subtracting thrust from the thrust minus nozzle drag term. Thrust at forward speeds is determined from the measured static thrust for each of the nozzle configurations (ref. 6). Nozzle drag includes both pressure and viscous forces.

Pressure Integrations. Nozzle flap and sidewall pressure drags were obtained by integrating pressures over the respective surfaces. Nozzle pressure drag is simply the sum of the flap and sidewall pressure drags. Note that these terms do not include nozzle friction drag which was approximately 0.0001 for all the nozzle tested. These terms will be used subsequently in the analysis of results.

Data Repeatability

Data for this investigation was acquired within a single wind tunnel entry of the model. Short-term repeatability has been quantified in terms of a 95% confidence level for nozzle N1. Examples of short term repeatability of integrated pressure drags are shown in figures 9 and 10 for nozzle N1 flap and sidewall pressure drag coefficients respectively at a Mach number of 0.90 for seven NPR sweeps. Four of the NPR sweeps were performed at the beginning of the test and the other 3 were taken at the end of the test period. These figures show the residuals of the integrated pressure drags defined as the difference in the individual measured data points from the estimated mean of the group of repeated NPR sweeps. The estimated mean was the average of the grouped data based on piecewise, 3rd order polynomial fits of the individual NPR sweeps. Also shown with the dashed lines, are the bounds of the 95% confidence interval as a function of NPR. In general, the residuals are small over the NPR range tested.

COMPUTATIONAL FLOW SOLVER

Governing Equation

The PAB computer code solves the three-dimensional, Reynolds-averaged Navier-Stokes (RANS) equations and uses one of several turbulence models for closure of the RANS equations. The governing equations are written in generalized coordinates and in conservative form. In an effort to decrease computational resources, simplified, thin-layer Navier-Stokes equations are implemented into PAB. This approximation neglects derivatives in the viscous terms streamwise and parallel to the surface, since they are typically negligible in comparison to the derivatives normal to the surface. Extensive details of PAB are found in references 7 and 8.

The flow solver was written with three numerical schemes: the flux vector scheme of van Leer (ref. 9), the flux difference-splitting scheme of Roe (ref. 10), and a modified Roe scheme used primarily for space marching solutions. These schemes implement the finite volume principle to balance the fluxes across grid cells and the upwind biased scheme of van Leer or Roe to determine fluxes at the cell interfaces. Only the inviscid terms of the flux vectors are split and the upwind differenced, while the diffusion terms of the Navier-Stokes equations are centrally differenced. The details and applications of these methods are given in references 7 and 8.

For this study and other typical three-dimensional simulations, the solutions are computed with the van Leer and Roe schemes. An iteration to steady state in a three-dimensional computational domain includes a forward and backward relaxation sweep in the streamwise direction, while implicitly updating each cross plane.

Turbulence Modeling

Turbulence modeling is required to predict solutions for many flow fields. The PAB code can perform several turbulence simulations by implementing either an algebraic or 2-layer, linear or nonlinear turbulence models. For this study, the Girimaji 2-equation, nonlinear Reynolds stress model (ref. 11) was chosen because this model has proven reliable in predicting propulsive flows with mixing, separated flow regions, and jet shear layers. A modified Jones and Launder form (ref. 12) of the damping function was utilized to treat the singularity at the wall. A high Reynolds number

model with no damping function was implemented in the free stream blocks.

Boundary Conditions

The PAB code allows for several boundary conditions at the inflow, outflow, free stream, and wall and centerline boundaries. Nozzle total temperature and total pressure with a normal fluid flow angle was used for the jet inflow boundary conditions. A jet total temperature of 528.67°R was used for all jet calculations. Riemann invariants along characteristics were used as inflow and free stream boundary conditions. A constant pressure for subsonic outflow was used far downstream as an outflow boundary condition. A no-slip adiabatic wall boundary was implemented to obtain viscous solutions

Performance Calculation

The PAB code contains a performance module (ref. 13) that utilizes the momentum theorem applied to a user-defined control volume to calculate nozzle or aerodynamic performance. Quantities such as lift, drag, thrust, moments, heat transfer and skin friction may be computed for many complex geometric configurations and multi-stream flows. Each quantity is updated throughout the solution development to monitor convergence

The skin friction force was calculated with only the velocity gradients normal to the surface contributing to the velocity term of the viscous stress tensor. A two point difference was used to determine the velocity gradients; one zero-magnitude velocity vector at the surface and the second at the cell center. Sutherland's formula was used to calculate the viscosity term at the surface by extrapolating the static temperature at a local cell center to the surface and using a reference viscosity and temperature condition.

Computational Procedure

The computational flow solving code PAB was used to predict solutions at Mach numbers 0.90 and 1.20 at a nozzle pressure ratio of 5 which was the design pressure ratio. Prediction of nozzle performance was done for nozzles N1 and N3.

The computational mesh was fully three-dimensional with 3 blocks defining the internal nozzle, and 9 blocks representing the free stream domain. The far field was located 10 body lengths upstream and downstream of the

aerodynamic nose and nozzle exit, respectively. The upper and lower lateral far field was located 6 body lengths above and below the aerodynamic body. The boundary layer was defined for a law-of-the-wall coordinate y^+ of 0.5 on the fine mesh spacing for adequate modeling of the boundary layer flow.

The base grid is a quarter plane representation of the experimental model with 1.57 million grid points in 9 blocks. Using a database reduction scheme, a cut 222 grid is generated by eliminating every other grid point in the i , j , and k directions. This cuts each grid dimension by 2, which decreases the grid count to 207,437 and substantially reduces the memory required to run the flow solver. The cut grid can also be sequenced in each direction for improved convergence rates and for grid assessment. For example, the flow solver uses alternating points in the i direction and every point in the j and k directions in a 211 sequence. Generally, a user would begin sequencing on the cut 222 grid. A pattern of 222, 221, 211, and then 111, or no sequencing might be used to assess solution behavior as more points are utilized in a particular direction. The solution is developed until convergence requirements are met at each level. Once the solution is converged on the cut 222 grid, the solution may be extrapolated to the base grid and sequencing may again be utilized.

For example, a converged solution was developed within 16.4 hours on a cut grid for nozzle N1 at $M=0.9$ and $NPR=5$. However, the solution was developed to the base level to quantify the effect of grid density. Nozzle drag decreased a mere 0.00002 in another 30 hours of computer time. Since the solution appears to be minimally dependent on doubling the grid density beyond the cut 222 level, the remaining solutions were developed by sequencing on the cut grid only. This allowed for quicker solution times due to the substantially smaller memory requirement.

DISCUSSION OF RESULTS

Experimental/Prediction Comparisons

Nozzle N1. A comparison between experimental and predicted pressures on flap F1 for nozzle N1 are presented in figure 11 at Mach numbers of 0.90 and 1.20 at $NPR = 5.0$. A nozzle pressure ratio of 5.0 was the design pressure ratio where the flow is expected to be fully expanded and peak nozzle internal

performance usually occurs. The boattail radius of curvature parameter was 0.40 for this flap and the sidewall was S1. Pressure distributions are compared along the flap centerline, and at the flap mid station, and at the flap outboard station. At $M = 0.90$, the CFD computations tend to over predict the expansion about the shoulder of the flap but do accurately predict the pressure recovery along the flap. As can be seen, the predicted pressures are in excellent agreement with experimental data at $M = 1.20$ at $NPR = 5$. In addition, the pressure distributions across the flap are nearly identical indicating that nearly uniform flow exists across the flap.

The experimental and predicted nozzle pressure drag coefficients are presented in figure 12 for nozzle N1 at $NPR = 5.0$. Shown in this figure are the flap, sidewall, and nozzle pressure drags where nozzle pressure drag is simply the sum of the sidewall and flap pressure drags. As would be expected from the excellent correlation of pressures, the predicted drags are in excellent agreement with experimental drag at $M = 0.9$ and within 0.3 of a drag count (one drag count equals 0.0001 drag coefficient) of experimental drag at $M = 1.2$.

A comparison of experimental and predicted nozzle total drag coefficients is presented in figure 13 where the nozzle total drag coefficient includes skin friction. Skin friction drag coefficient for the prediction is computed within the performance module of the PAB code. The skin friction drag coefficient $C_{D,f}$ is determined using the Frankl-Voishel skin friction coefficient as part of the wind tunnel standard data reduction system (ref. 6). The measured drag coefficient is obtained from the force data measurements. As was the case for the pressure drag coefficients, excellent agreement exists. The total drag coefficients agree to within one half drag count (0.00005) at $M = 0.90$ and one drag count (0.0001) at 1.20.

Nozzle N3. Experimental and predicted pressure distribution comparisons for nozzle N3 are shown in figure 14. The boattail radius of curvature parameter was 0 for this flap that meant it had a sharp corner at the start of the boattail. As can be seen, the agreement between the experimental and predicted pressures is not as good as was the case for nozzle N1 at $M = 0.90$. Consequently, there is poor correlation of the flap pressure drag (fig. 15) and nozzle total drag coefficient (fig. 16). One possible reason for this poor agreement may be that the model flap had a

small radius at the shoulder. Treatment of the corner flow is critical computationally at speeds less than Mach number 1. However, at $M = 1.20$, where geometrically matching the corner is not as critical, agreement between the experimental and predicted pressures was similar to nozzle N1.

Effect of Nozzle Boattail Curvature

The effects of varying nozzle boattail radius of curvature on flap and sidewall pressure drag and on nozzle pressure drag are presented in figures 17 and 18 respectively. These nozzles all had the baseline flap length $L_f/h_m = 1.4$ and were tested with sidewall S1. Results are presented at a nozzle pressure ratio of 5.0 that was the design pressure ratio. Although discussion of results at this pressure ratio would generally be applicable to other pressure ratios, the relative difference between comparisons may vary. Figure 17 also illustrates the typical breakdown of pressure drag between the nozzle flaps and the sidewalls. Generally, varying flap geometry had little or no effect on sidewall pressure drag. The breakdown of the pressure drags is similar for the other nozzle configurations tested.

The lowest nozzle pressure drag was obtained on nozzle N3 with flap F3 that had no radius of curvature (fig 18). This was an unexpected result because previous experience has shown that axisymmetric nozzles with a sharp shoulder generally have higher drag (ref. 2). However, these nozzles generally had shorter external flaps and were designed for use with subsonic cruise vehicles. In order to try to understand this result, one can examine the pressure distributions on these nozzles.

Pressure distributions along the centerline row of the top flap for nozzles N1, N2, N3, and N4 are presented at $M = 0.90$ and 1.20 at $NPR = 5$ in figure 19. Basically what is shown is that even though nozzle N3 with no curvature had the greatest expansion of flow about the nozzle shoulder, it had better pressure recovery characteristics than the other three nozzles. Similar results were found for the pressure distributions along both the mid and outboard pressure rows (not shown).

Figure 20 shows flap pressure drag for the two nozzles tested with the smaller flap lengths. Except at $M = 1.20$, these two nozzles followed similar trends as the nozzles with the longer flap lengths. At $M = 0.90$ and 0.95 , nozzle pressure drag decreased as the radius of curvature parameter was increased from 0.1 to 0.4.

Effect of Nozzle Flap Length

Varying the length of nozzle the flap is illustrated in figure 21 where nozzle pressure drag is compared between nozzle N2 and N6. Each of these nozzles had a radius of curvature parameter of 0.1. As can be seen, the nozzle with the longer nozzle flap had lower drag at all the Mach numbers tested. This was probably due to nozzle N2 having a lower boattail angle.

Results similar to those shown in the previous figure were also obtained for nozzles N1 and N5. These nozzles had a curvature ratio of 0.4.

Effect of Sidewall Boattail Angle

The effects of varying sidewall boattail angle on sidewall and flap pressure drag and nozzle pressure drag are summarized in figures 22 and 23. There are no definite trends to changing sidewall boattail angle. For example, at $M = 0.80$ and 0.90 , nozzle N6 with sidewall S3 and $\beta_s = 8^\circ$ had the lowest sidewall pressure drag whereas, just the opposite was true at $M = 1.20$. At $M = 0.90$ (fig. 24), it is interesting to note that although sidewall S3 exhibited greater expansion of the flow about the boattail than sidewall S1, it exhibited somewhat better recovery such that this sidewall had lower pressure drag. Figure 24 also shows that the flow across the sidewall is somewhat nonuniform in nature since expansion outboard about the boattail is greater for all the sidewalls than at the center of the sidewall. However, flow recovers to about the same pressure coefficient levels at both locations.

At $M = 1.20$, sidewall pressure drag for nozzle N6 with sidewall S4 was doubled that of nozzle N1 with sidewall S1 as sidewall drag increased from 0.00017 to 0.00035 (fig. 22). Examination of the pressure distributions of figure 25 at this Mach number reveals markedly different flow characteristics across the sidewall. Along the center of the sidewall, the flow is rather benign and shows relatively little differences as β_s increased from 4° to 6° . Outboard on the sidewall, there is a rapid expansion of the flow about the shoulder for each of the boattail angles tested. The data indicates possible flow separation for the sidewalls with 6° and 8° boattail angles. Although the full-scale nozzle was design to have a sidewall with 4° boattail, it became evident as the HSR program progressed, sidewalls with boattail angles greater than 4°

may be needed for both structural needs and to house nozzle actuation hardware. This could pose a problem at supersonic cruise where the potential now exists for even greater values of sidewall pressure drag to occur because of sidewall boattail angles greater than 4° .

Only at $M = 0.95$, did changing boattail angle appreciably affect flap pressure drag (fig. 22). Flap pressure drag coefficient increased 0.00011 as boattail angle increased from 4° to 6° , which was twice as large as the increase in sidewall pressure drag. This is a somewhat surprising result in that one would not expect such a strong effect of varying sidewall geometry on flap performance. This is because the full height sidewalls tend to act like fences and isolate the sidewall flow from the flow over the flap.

Effect of Sidewall Boattail Curvature

Several sidewalls were tested with varying amounts of curvature with both 6° and 8° boattail angles. Some typical results for those nozzles N6, N8, and N10 with $\beta_S = 8^\circ$ are shown in figure 26. Sidewall pressure drag decreased by 0.00014 as the $r_S / r_{S,max}$ was increased from 0 to 1.0 at $M = 1.20$. This could prove to be significant if sidewall with boattail angles greater than 4° are needed as discussed previously. Sidewalls with full curvature would be feasible for the full-scale aircraft since the sidewalls are fixed.

Similar results (not shown) were obtained for those nozzles with $\beta_S = 6^\circ$ except that variations in sidewall pressure drag were less than for those nozzles with $\beta_S = 8^\circ$. These were nozzles N5, N7, and N9 with sidewalls S2, S4 and S4 respectively.

Effect of Sidewall Height

The height of the sidewall was fixed so that the nozzle internal flaps would not unport in the supersonic cruise position. As such, the sidewalls are very large unsupported panels that account for about 60-percent of the nozzle skin friction drag. To assess what drag penalties might occur with the full height sidewalls, some tests were performed with reduced height or cutback sidewalls. The height of the cutback sidewall S8 was contoured to match the external shape of flap F1. Sidewall S8 was then tested with flaps F1 and F2 to form nozzles N11 and N12 respectively (fig. 5).

Sidewall and flap pressure drag and nozzle pressure drag coefficients for nozzle N1 and N11 are presented in figures 27 and 28 respectively. Significant reductions in both sidewall and flap pressure drag were obtained for the cutoff sidewall over the entire Mach number test range. For example, at $M = 0.90$, there was a 0.00012 reduction in nozzle pressure drag coefficient $C_{D,p}$ and a 0.00023 reduction in $C_{D,p}$ at $M = 1.20$. This would be equivalent to at least a 0.00092 reduction in drag coefficient for the HSCT vehicle with four engines. This does not include a small reduction in skin-friction drag.

The flow characteristics over the nozzle flap are different for the two sidewalls. With the reduced height sidewall, the flow along the sidewall tends to accelerate around the corner onto the flap where it can become highly three-dimensional. The full height sidewalls tend to act like fences in inhibiting any communication between the sidewall and flap flows, which results in the flow over the flap being more uniform. This can be seen in figure 29 where pressure distributions along the flap centerline and outboard rows are shown for a Mach number of 0.90.

Similar results (not shown) were also obtained for nozzle N12; however, the reduction in pressure drag was smaller than that noted for nozzle N11.

CONCLUSIONS

The results of this investigation indicate the following:

1. Excellent correlation between experimental and CFD results were obtained for the nozzle with a moderate amount of boattail curvature.
2. The nozzle with an external flap having a sharp shoulder (no curvature) had the lowest nozzle pressure drag.
3. At a Mach number of 1.2, sidewall pressure drag doubled as sidewall boattail angle was increased from 4° to 8° .
4. Reducing the height of the sidewall caused large decreases in both the sidewall and flap pressure drags.

REFERENCES

1. Wilhite, Allan W.; and Shaw, Robert J.: *An Overview of NASA's High Speed Research Program*. 20th ICAS Congress, Paper112, August 2000.
2. Stitt, Leonard E.: *Exhaust Nozzles for Propulsion Systems with Emphasis on Supersonic Cruise Aircraft*. NASA RP-1235, May 1990.
3. Wallace, Hoyt; et al: *Isolated and Installed Nozzle Boattail Drag Studies*. NASA/CP-1999-209691/VOL1/PT1. December 1999.
4. Capone, Francis J.; Bangert, Linda S.; Asbury, Scott C.; Mills, Charles T.; and Bare, E. Ann: *The NASA Langley 16-Foot Transonic Tunnel - Historical Overview, Facility Description, Calibration, Flow Characteristics, Test Capabilities*. NASA TP-3521, 1995.
5. Capone, Francis J.; Re, Richard J.; and Bare, E. Ann: *Parametric Investigation of Single-Expansion Ramp Nozzles at Mach Numbers From 0.60 to 1.20*. NASA TP-3240, October 1992.
6. Mercer, Charles E.; Berrier, Bobby L.; Capone, Francis J.; and Grayston, Alan M.: *Data Reduction Formulas for the Langley 16-Foot Transonic Tunnel: NASA Langley Research Center*. NASA TM-107646, 1992.
7. Abdol-Hamid, Khaled S.: *Application of a Multiblock/Multizone Code (PAB) for the Three-Dimensional Navier-Stokes Equations*. AIAA-91-2155, June 1991.
8. Abdol-Hamid, Khaled S.: *Implementation of Algebraic Stress Models in a General 3-D Navier-Stokes Method (PAB)*. NASA CR-4702. 1995.
9. van Leer, B.: *Flux-Vector Splitting for the Euler Equations*. ICASE 1Report 82-30, 1982.
10. Roe, P.L.: *Characteristics Based Schemes for the Euler Equations*. A Numerical Review of Fluid mechanics, 1986, pp. 337-365.
11. Girimaji, S. S.: *Fully-Explicit and Self-Consistent Algebraic Reynolds Stress Model*. ICASE 95-82, December 1995.
12. Jones, W.P.; and Launder, B.E.: *The Prediction of Laminarization with a Two-Equation Model of Turbulence*. Int. J. Heat & Mass Trans., vol. 15, no. 2, Feb. 1972, pp. 301-314.
13. Carlson, John R.: *A Nozzle Internal Performance Prediction Method*. NASA TP-3221, 1992.

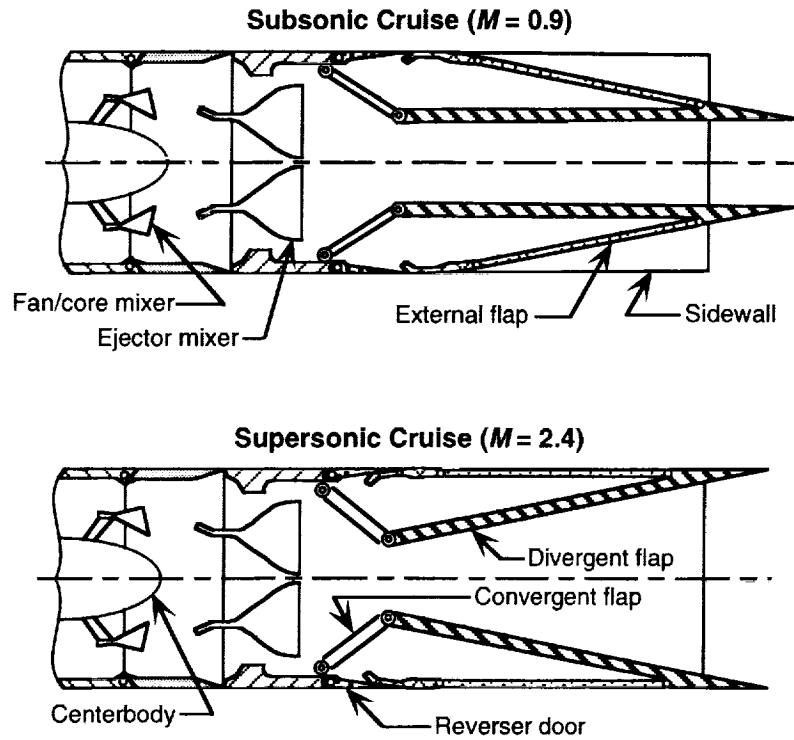


Figure 1. Sketches of full-scale nozzle concept at two flight conditions.

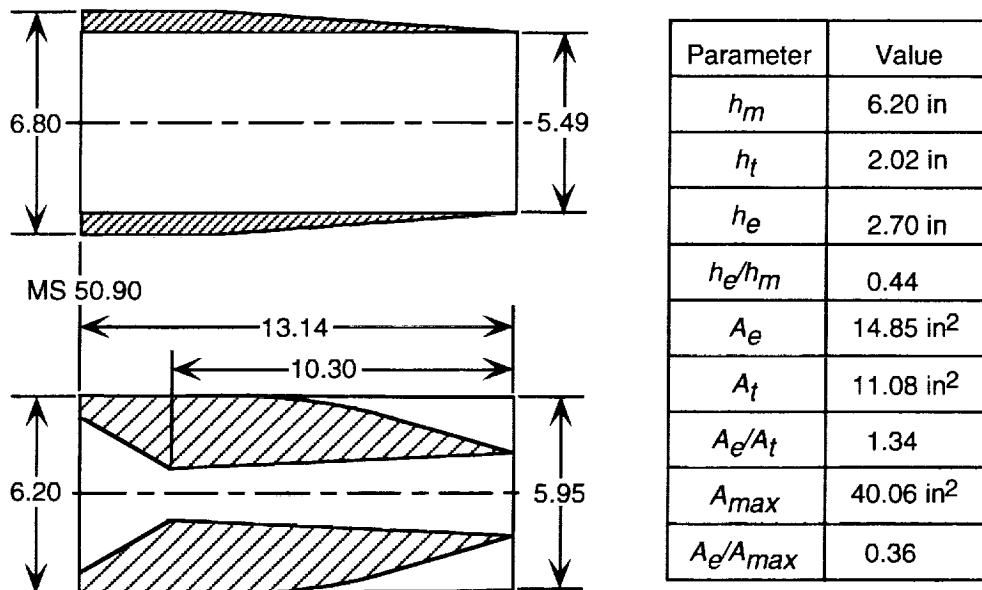
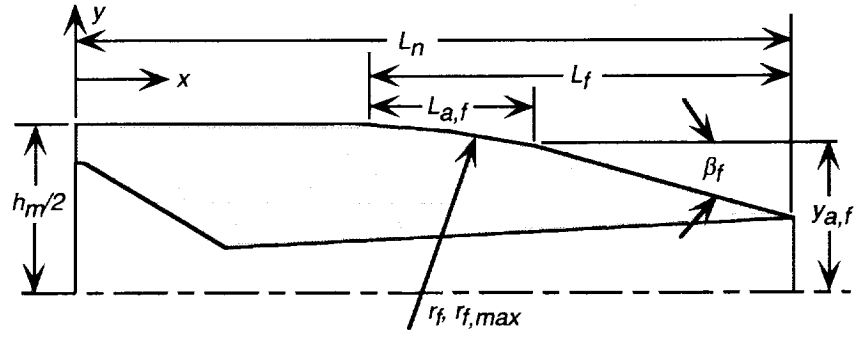
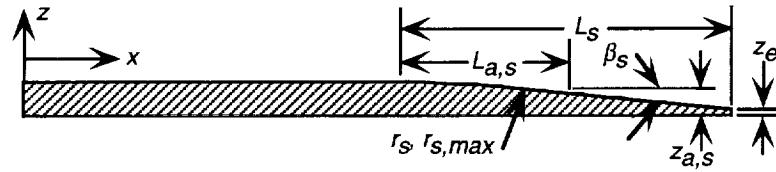


Figure 2. Overall nozzle geometry. All dimensions in inches.



Nozzle flap						
Parameter	F1	F2	F3	F4	F5	F6
L_f/h_m	1.4	1.4	1.4	1.4	1.1	1.1
$r_f/r_{f,max}$	0.4	0.1	0	1.0	0.4	0.1
β_f deg	16.38	12.88	11.72	23.44	20.30	15.97
L_n in	13.14	13.14	13.14	13.14	13.14	13.14
L_f in	8.42	8.42	8.42	8.42	6.74	6.74
$L_{a,f}$ in	4.86	1.55	0.0	8.42	3.90	1.24
$y_{a,f}$ in	2.40	2.92	3.1	1.35	2.40	2.92
r_f in	17.22	6.94	0.0	21.18	11.26	4.52

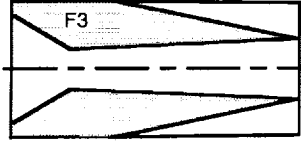
Figure 3. Definition of flap geometric parameters.



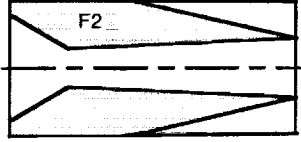
Sidewall								
Parameter	S1	S2	S3	S4	S5	S6	S7	S8
β_s deg	4	6	8	6	8	6	8	4
$r_s/r_{s,max}$	0.0	0.0	0.0	0.1	0.1	0.4	1.0	0.0
L_s in	9.06	6.02	4.51	6.63	4.96	7.36	9.06	9.06
$L_{a,s}$ in	0.0	0.0	0.0	1.21	0.91	4.21	9.06	0.0
$z_{a,s}$ in	0.65	0.65	0.65	0.59	0.59	0.43	0.02	0.65
z_e in	0.02	0.02	0.02	0.02	0.02	0.10	0.02	0.02
r_s in	0.0	0.0	0.0	11.56	6.51	40.29	6.51	0.0

Figure 4. Definition of sidewall geometric parameters.

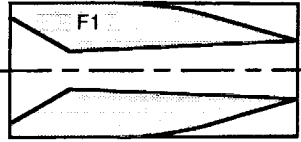
Nozzles with $L_f/h_m = 1.4$, sidewall S1



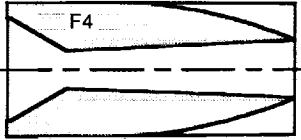
Nozzle N3, $r_f/r_{f,max} = 0$



Nozzle N2, $r_f/r_{f,max} = 0.1$

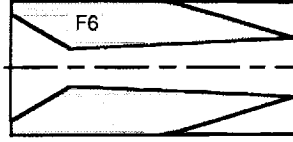


Nozzle N1, $r_f/r_{f,max} = 0.4$

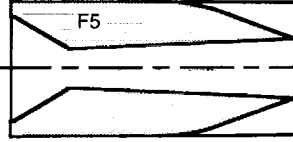


Nozzle N4, $r_f/r_{f,max} = 1.0$

Nozzles with $L_f/h_m = 1.1$, sidewall S1

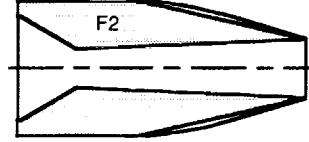


Nozzle N14, $r_f/r_{f,max} = 0.1$

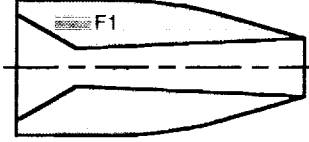


Nozzle N13, $r_f/r_{f,max} = 0.4$

Nozzles with $L_f/h_m = 1.4$, sidewall S8



Nozzle N12, $r_f/r_{f,max} = 0.1$



Nozzle N11, $r_f/r_{f,max} = 0.4$

Figure 5. Sketches of nozzles with various flaps tested.

Nozzles with $r_s/r_{s,max} = 0$



Nozzle N1, $\beta_f = 4^\circ$

Nozzles with $\beta_f = 6^\circ$



Nozzle N5, $r_s/r_{s,max} = 0$

Nozzles with $\beta_f = 8^\circ$



Nozzle N6, $r_s/r_{s,max} = 0$



Nozzle N5, $\beta_f = 6^\circ$



Nozzle N7, $r_s/r_{s,max} = 0.1$



Nozzle N8, $r_s/r_{s,max} = 0.1$



Nozzle N6, $\beta_f = 8^\circ$



Nozzle N9, $r_s/r_{s,max} = 0.4$



Nozzle N10, $r_s/r_{s,max} = 1.0$

Figure 6. Sketches of nozzles with various sidewalls tested.

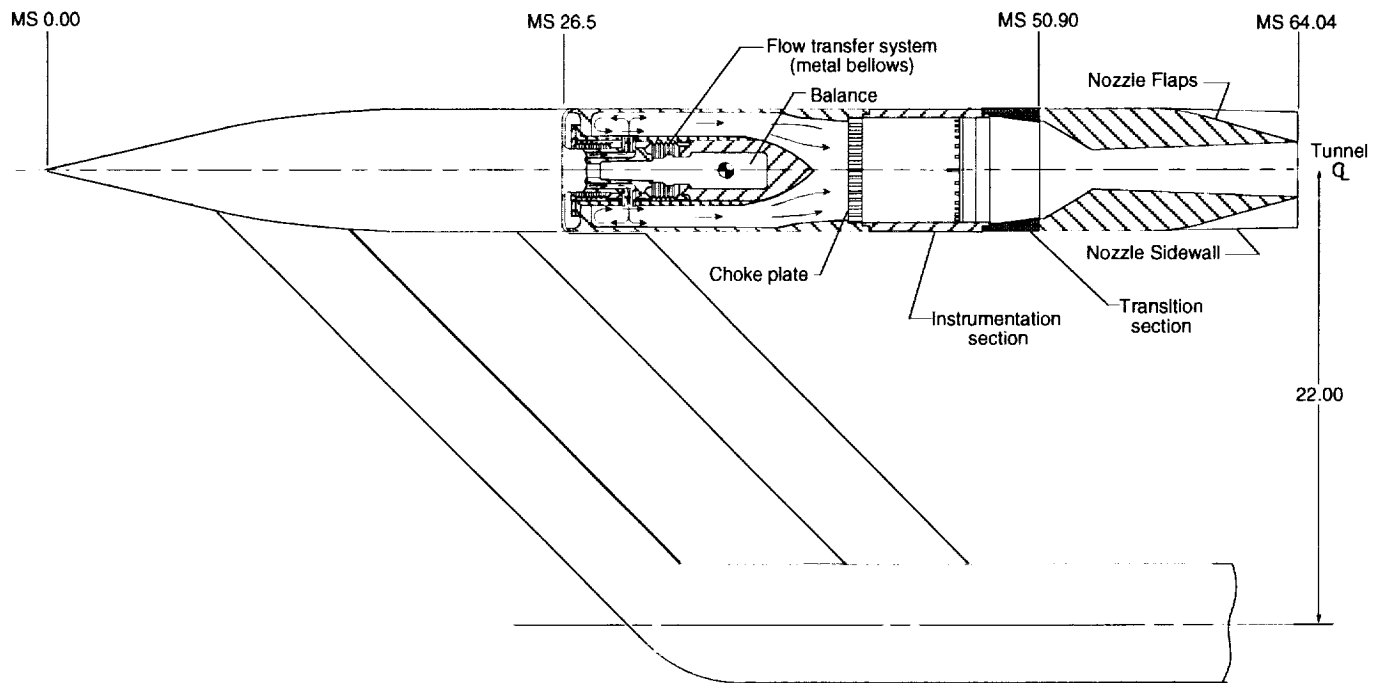


Figure 7. Single engine propulsion simulator.

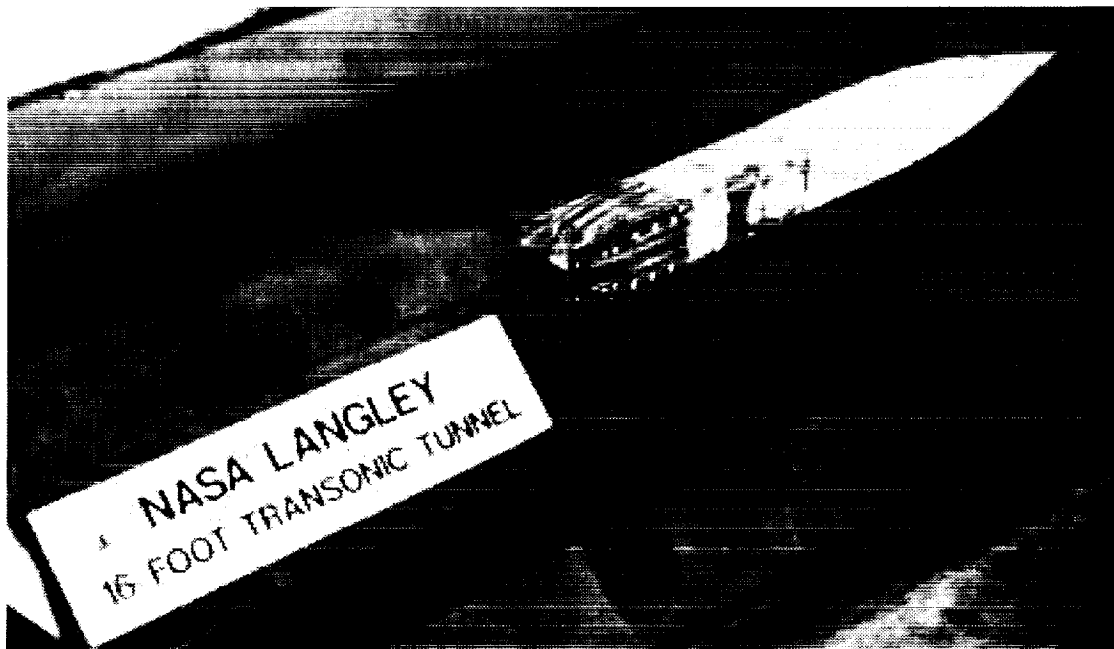


Figure 8. Photograph of model.

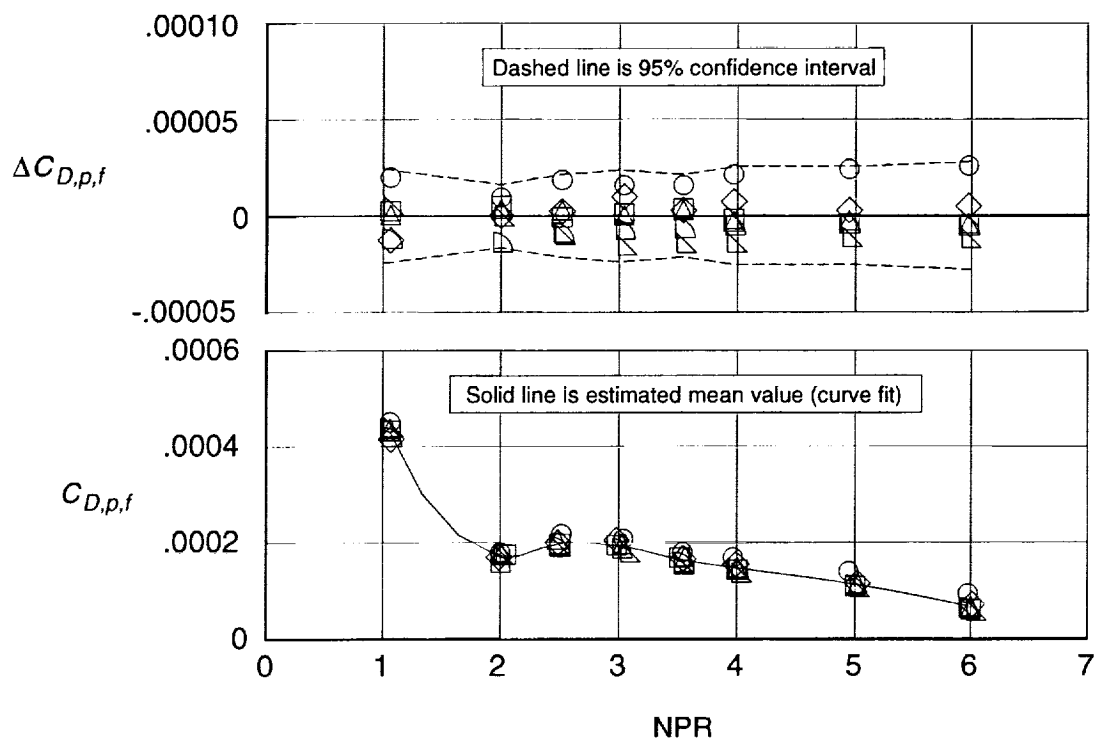


Figure 9. Short term repeatability for flap pressure drag coefficient, nozzle N1, $M = 0.90$.

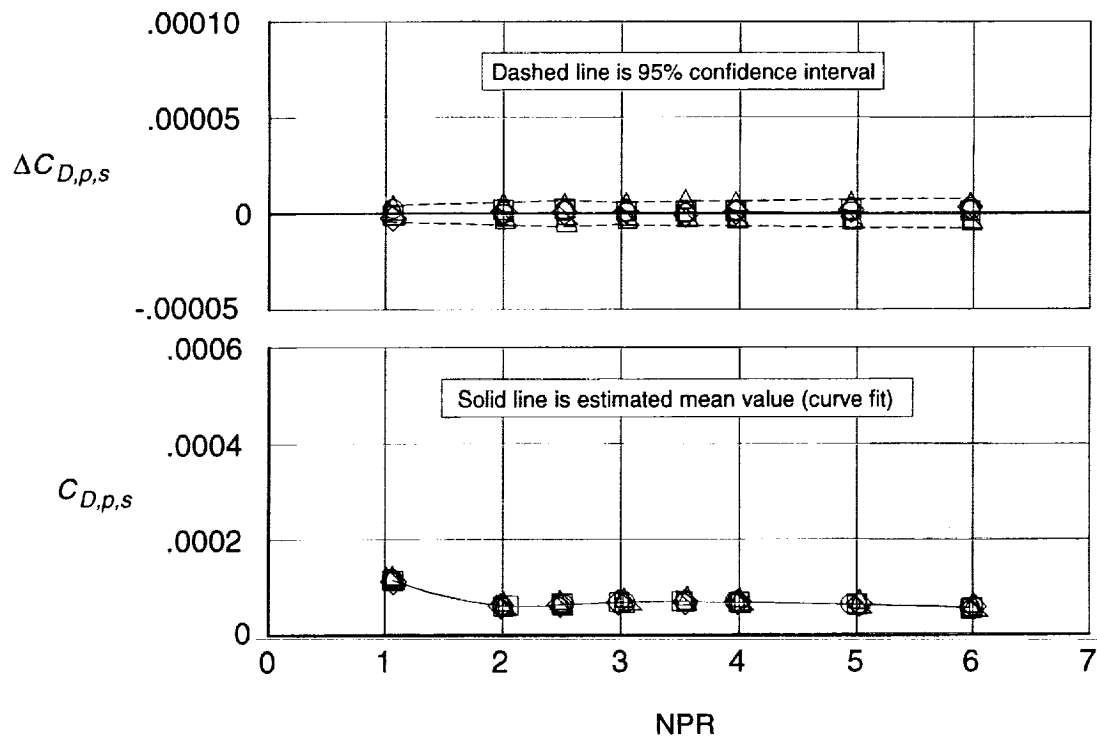


Figure 10. Short term repeatability for sidewall pressure drag coefficient, nozzle N1, $M = 0.90$.

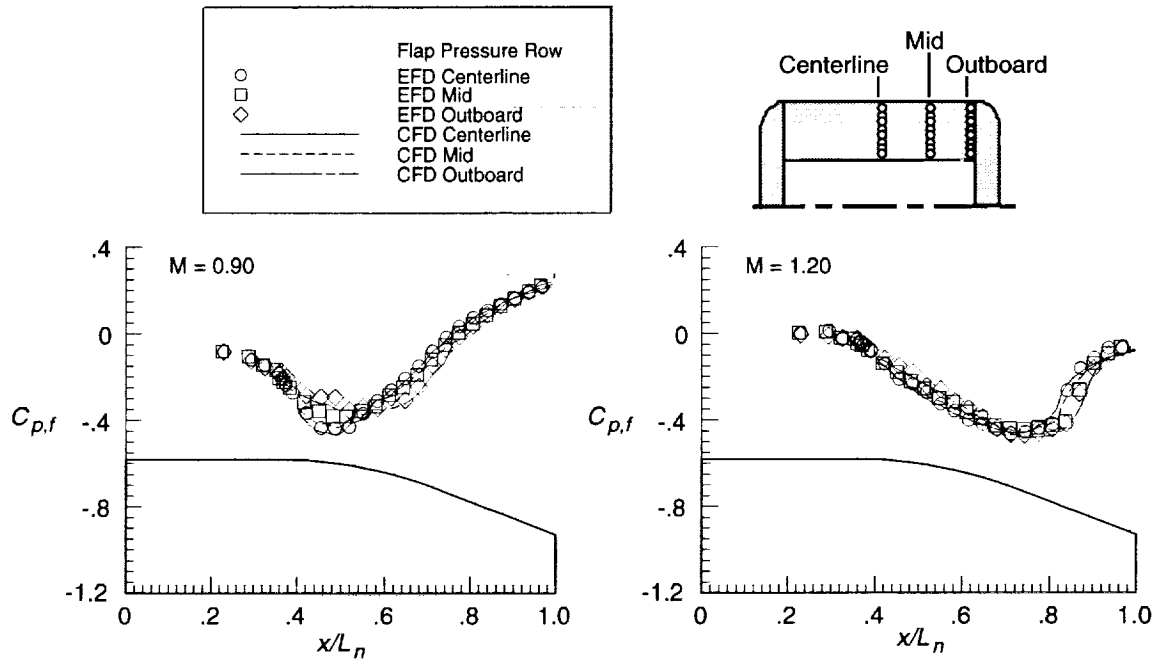


Figure 11. Comparison of experimental and predicted pressure coefficients for Nozzle N1, $NPR = 5$, $L_f/h_m = 1.4$, $\beta_f = 16.38^\circ$, $r_f/r_{f,max} = 0.4$.

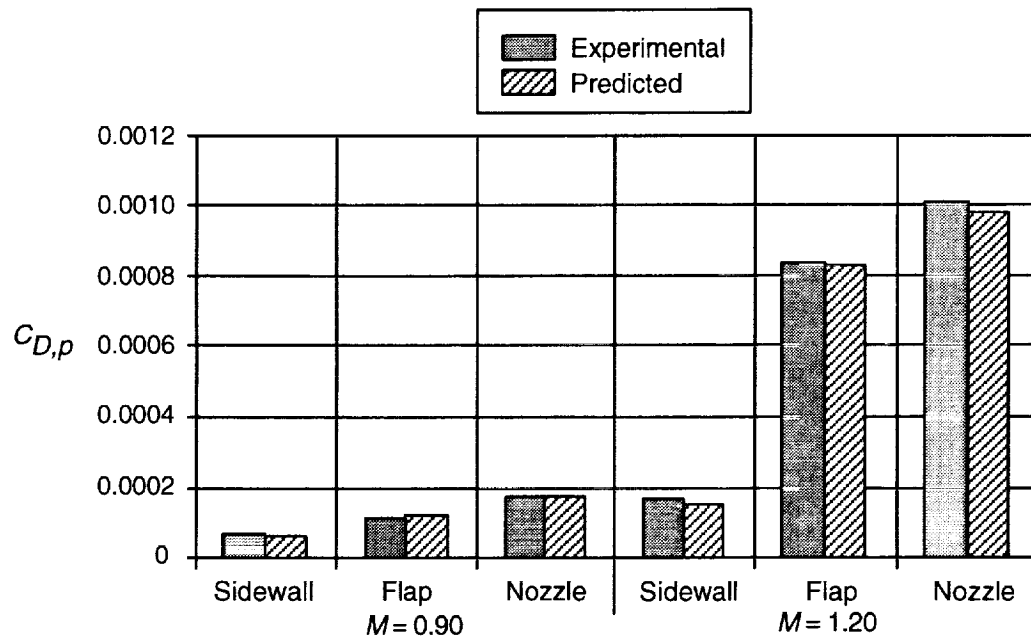


Figure 12. Comparison of experimental and predicted pressure drags for Nozzle N1, $NPR = 5$, $L_f/h_m = 1.4$, $\beta_f = 16.38^\circ$, $r_f/r_{f,max} = 0.4$.

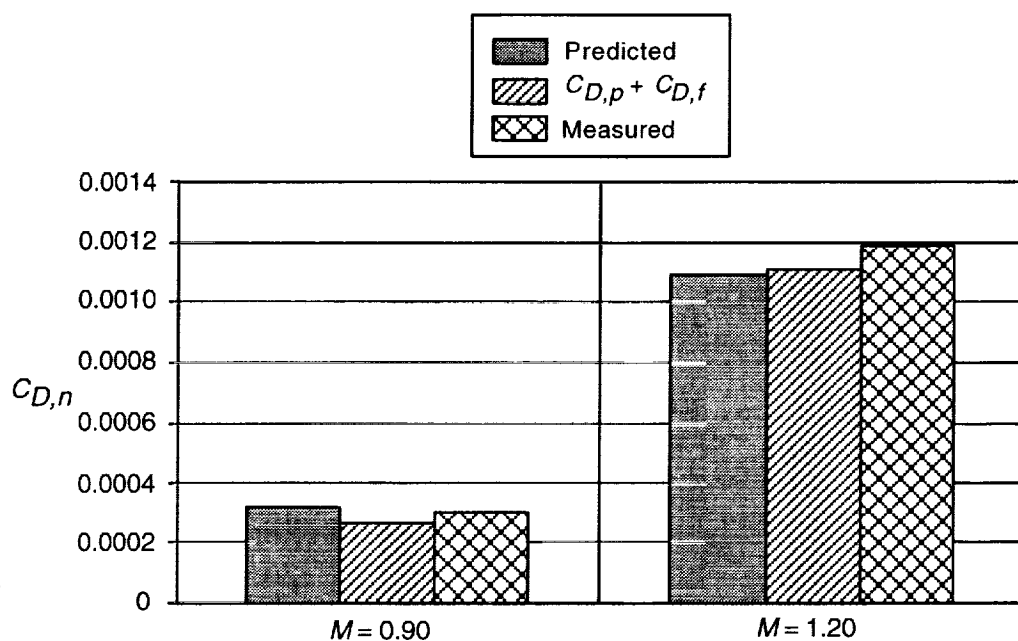


Figure 13. Comparison of experimental and predicted total drag for Nozzle N1, NPR = 5, $L_f/h_m = 1.4$, $\beta_f = 16.38^\circ$, $r_f/r_{f,max} = 0.4$.

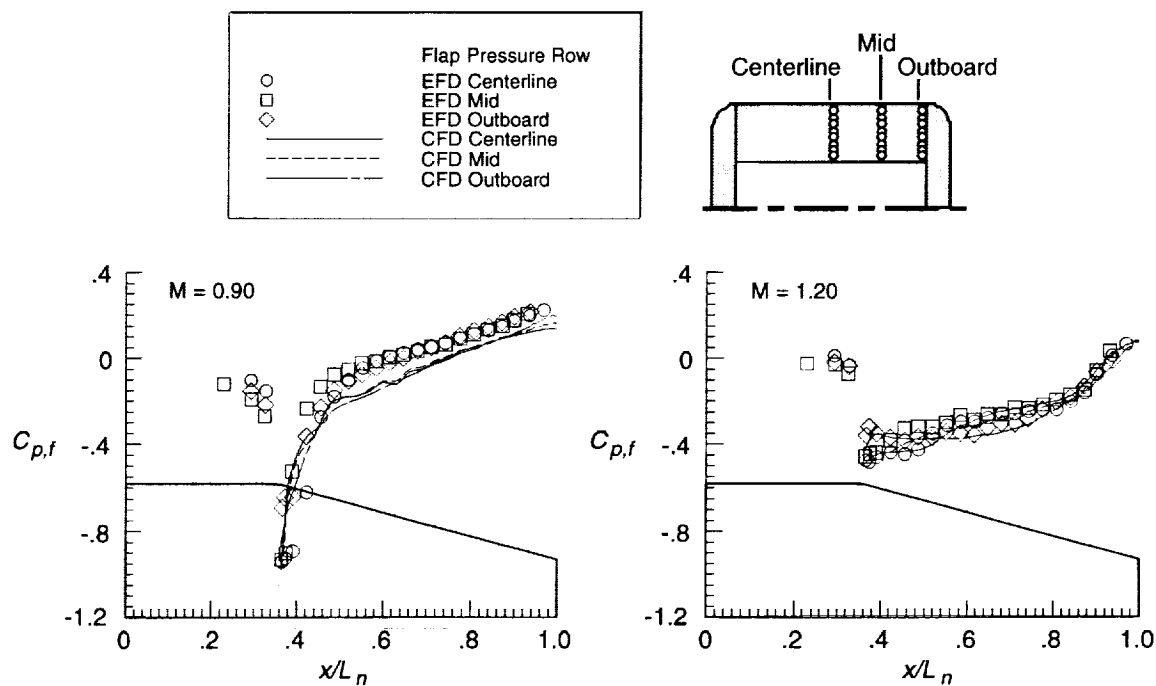


Figure 14. Comparison of experimental and predicted pressure coefficients for Nozzle N3, NPR = 5, $L_f/h_m = 1.4$, $\beta_f = 11.72^\circ$, $r_f/r_{f,max} = 0$.

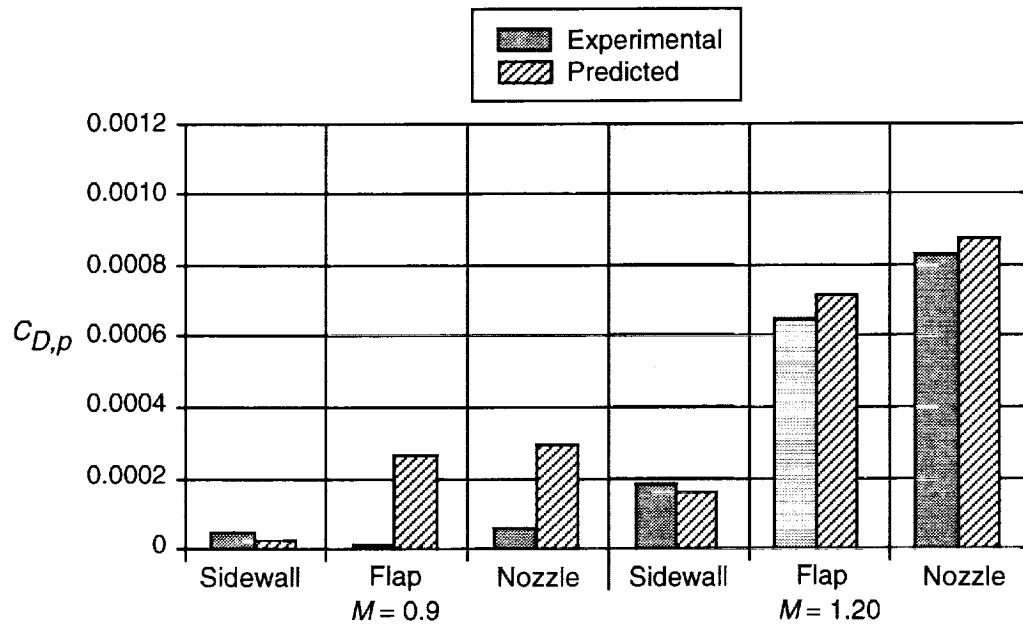


Figure 15. Comparison of experimental and predicted pressure drags for Nozzle N3, NPR = 5, $L_f/h_m = 1.4$, $\beta_f = 11.72^\circ$, $r_f/r_{f,max} = 0$.

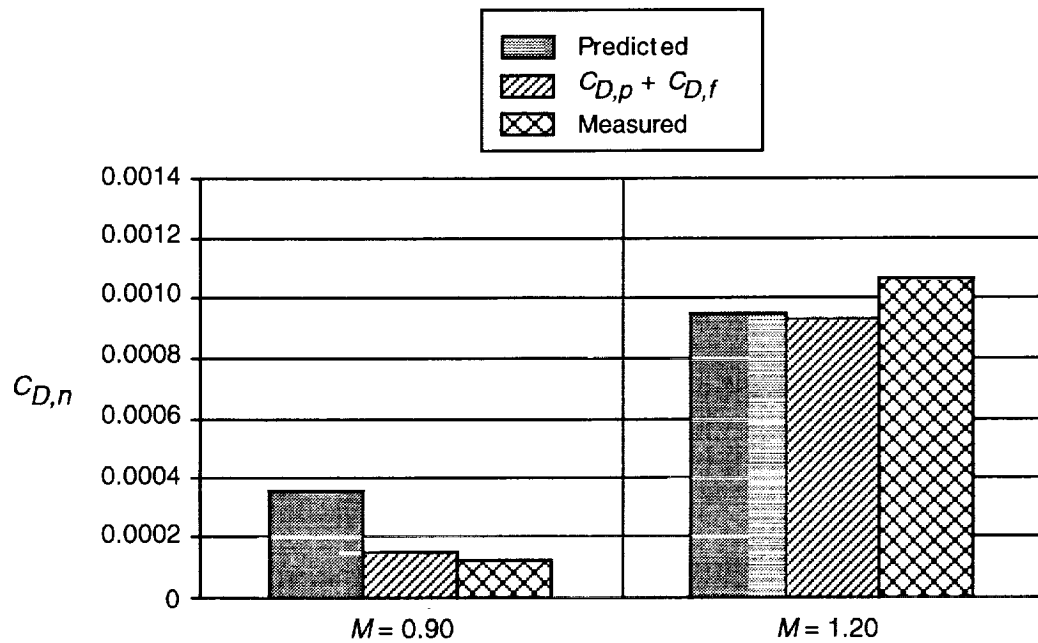


Figure 16. Comparison of experimental and predicted total nozzle drag for Nozzle N3., NPR = 5, $L_f/h_m = 1.4$, $\beta_f = 11.72^\circ$, $r_f/r_{f,max} = 0$.

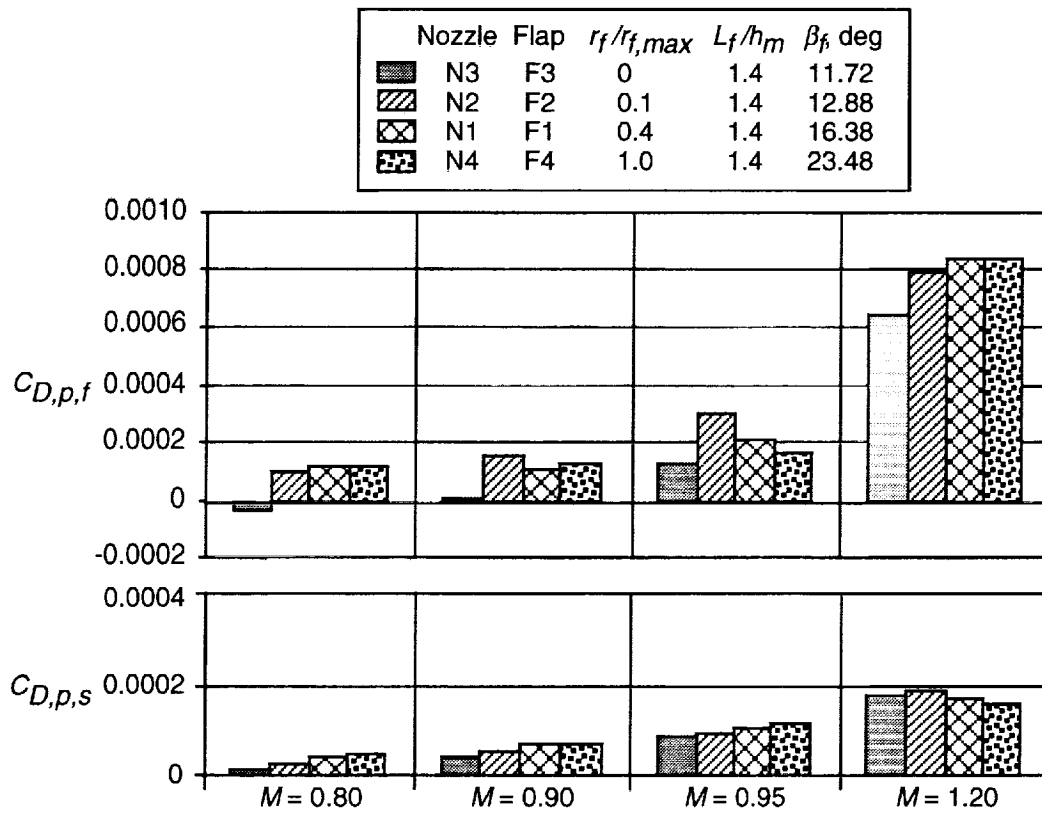


Figure 17. Effect of flap radius of curvature on nozzle pressure drag, NPR = 5.

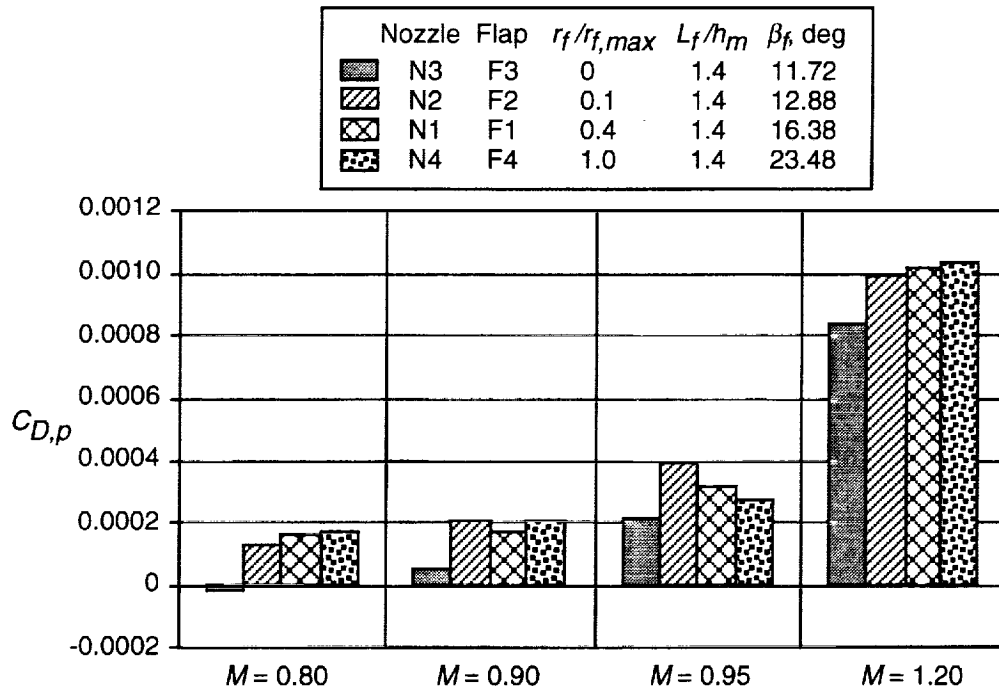


Figure 18. Effect of flap radius of curvature on nozzle pressure drag, NPR = 5.

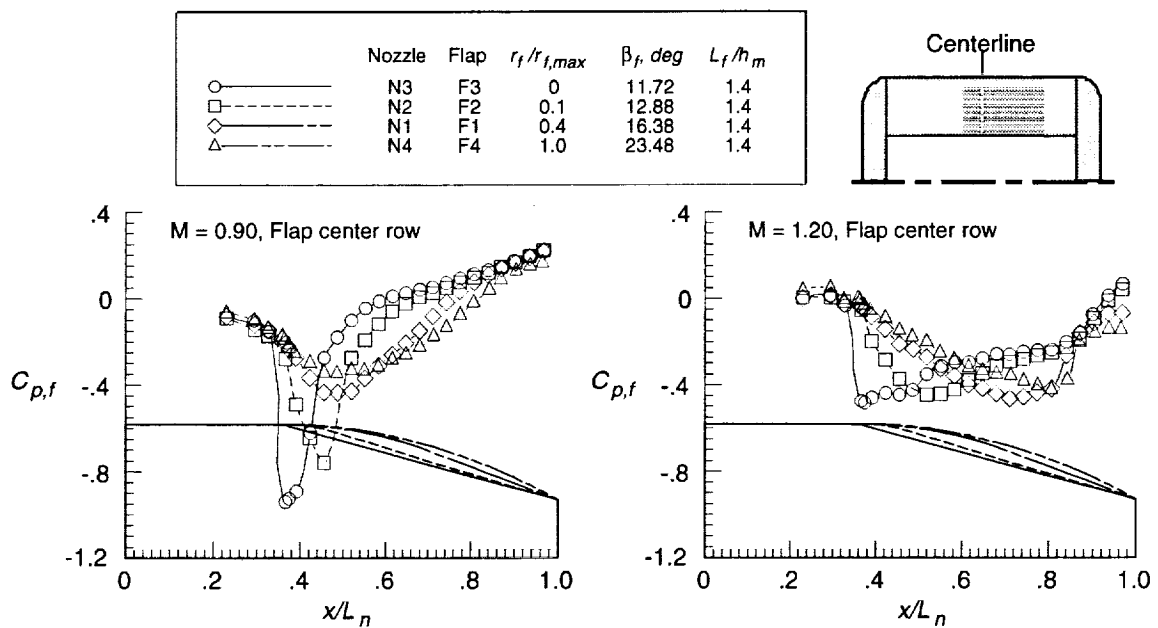


Figure 19. Effect of flap radius of curvature on pressure distributions, NPR = 5.

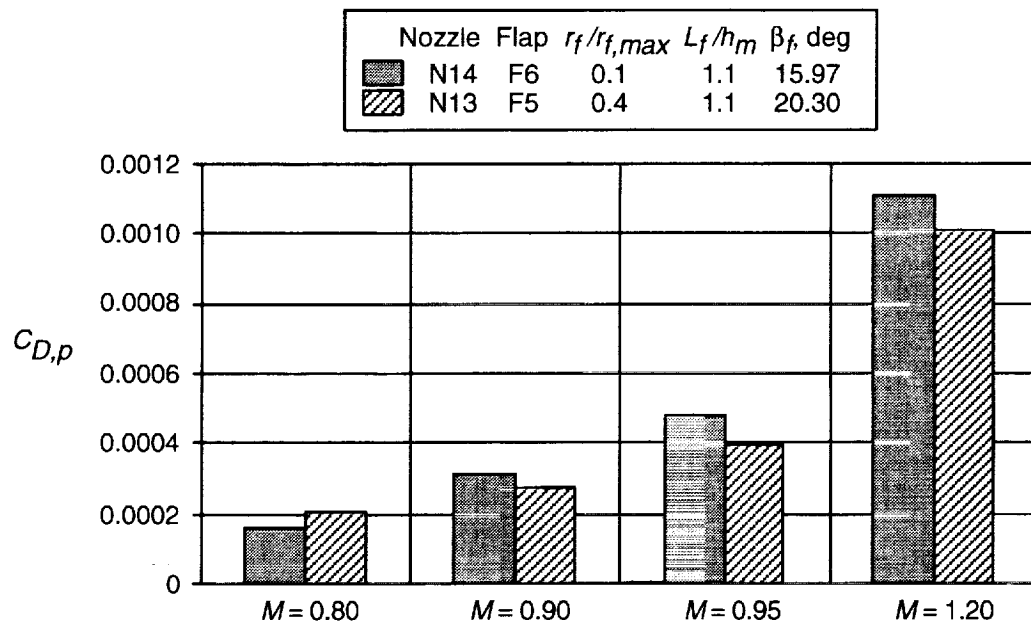


Figure 20. Effect of flap radius of curvature on nozzle pressure drag, NPR = 5.

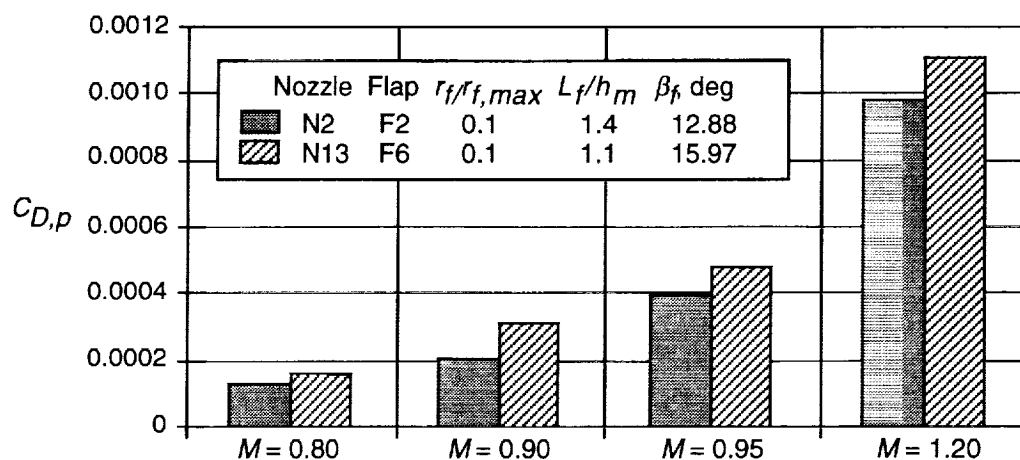


Figure 21 Effect of flap length on nozzle pressure drag, NPR = 5.0.

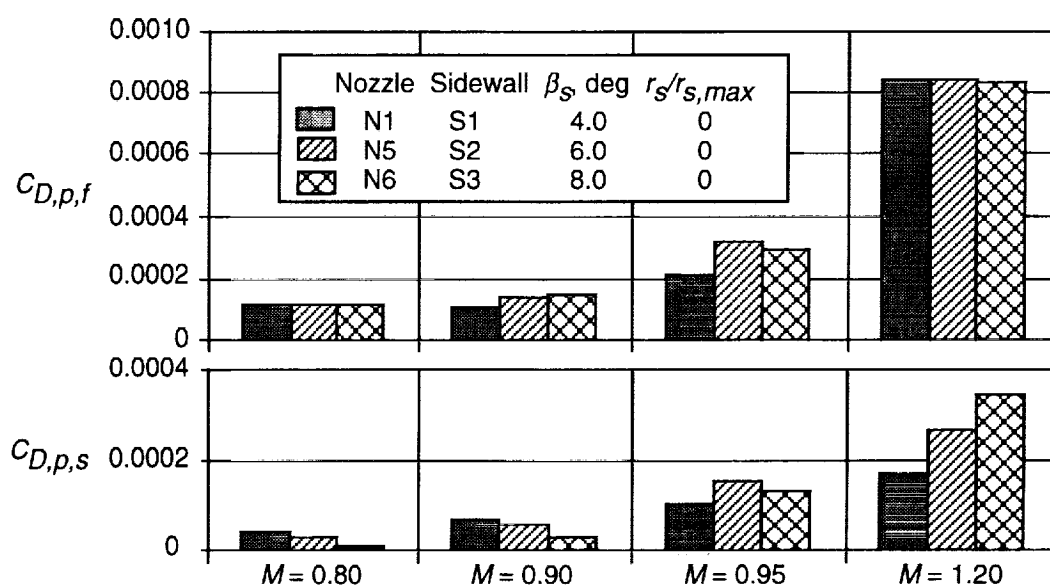


Figure 22. Effect of sidewall boattail angle on flap and sidewall pressure drag, NPR = 5.0.

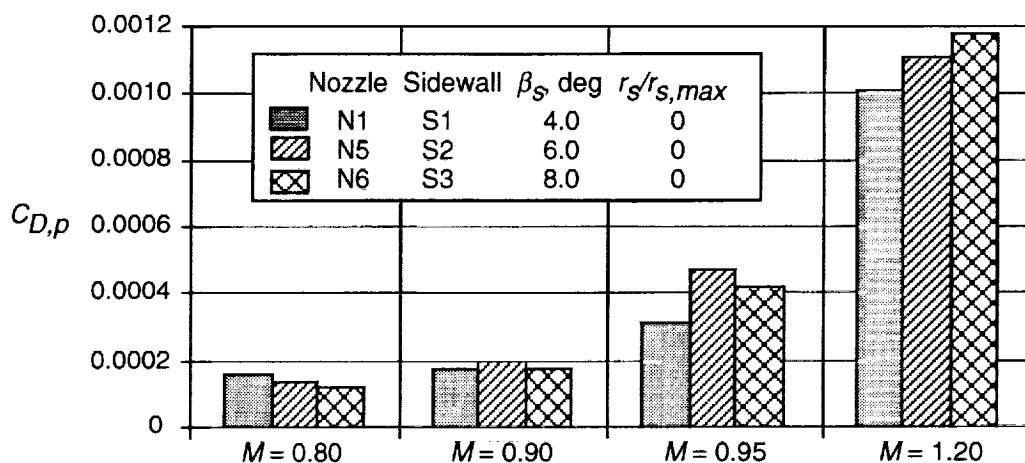


Figure 23. Effect of sidewall boattail angle on nozzle pressure drag, NPR = 5.0.

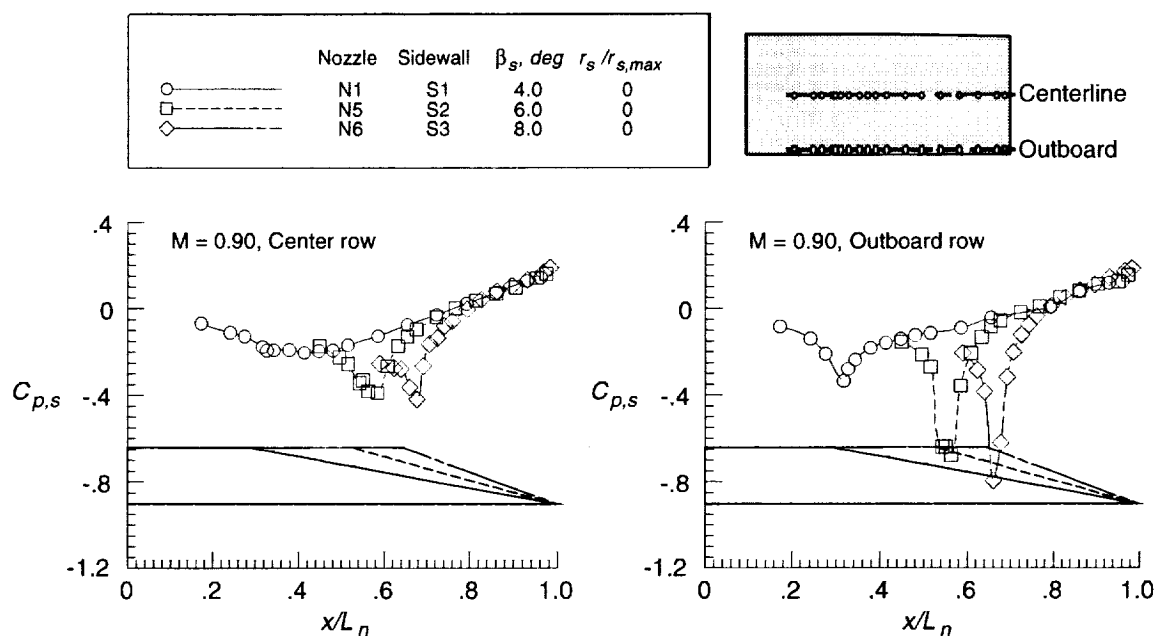


Figure 24. Effect of sidewall boattail angle on pressure distributions, $M = 0.90$, NPR = 5.

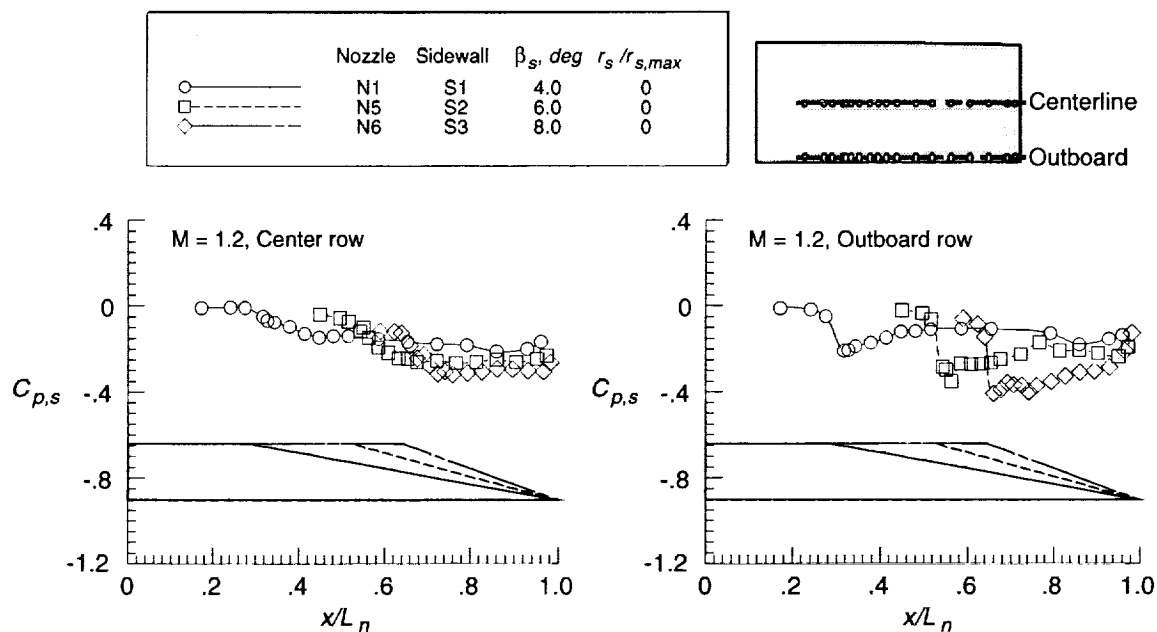


Figure 25. Effect of sidewall boattail angle on pressure distributions, $M = 1.2$, NPR = 5.

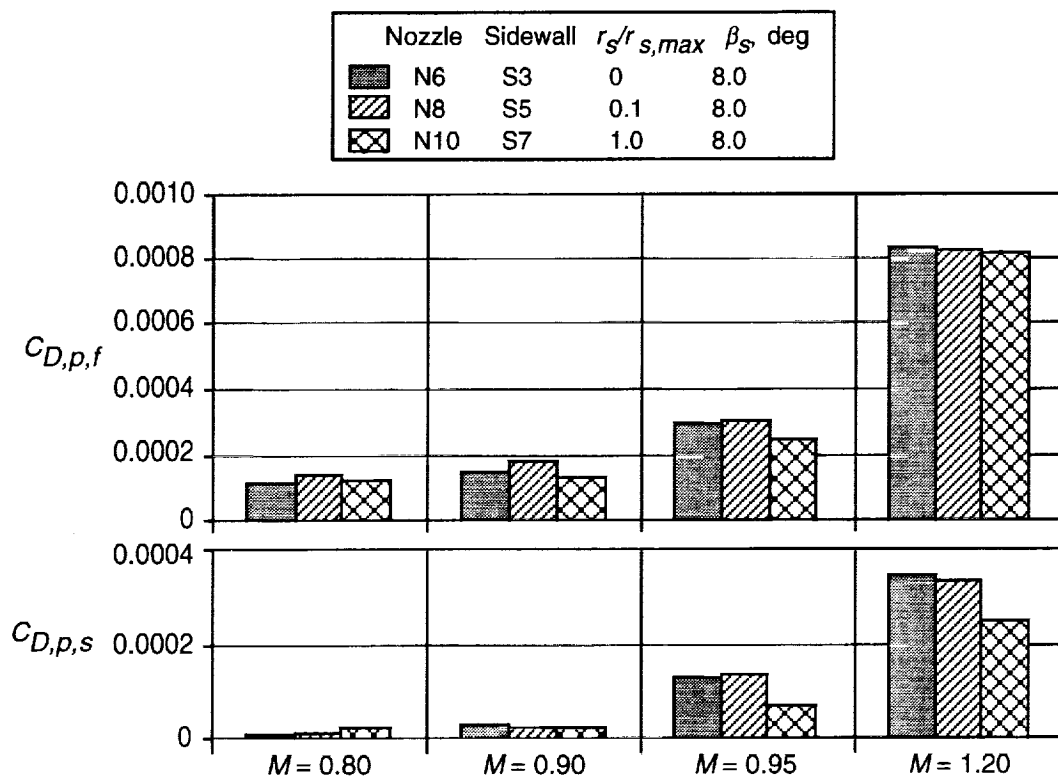


Figure 26. Effect of sidewall radius of curvature on flap and sidewall pressure drag.

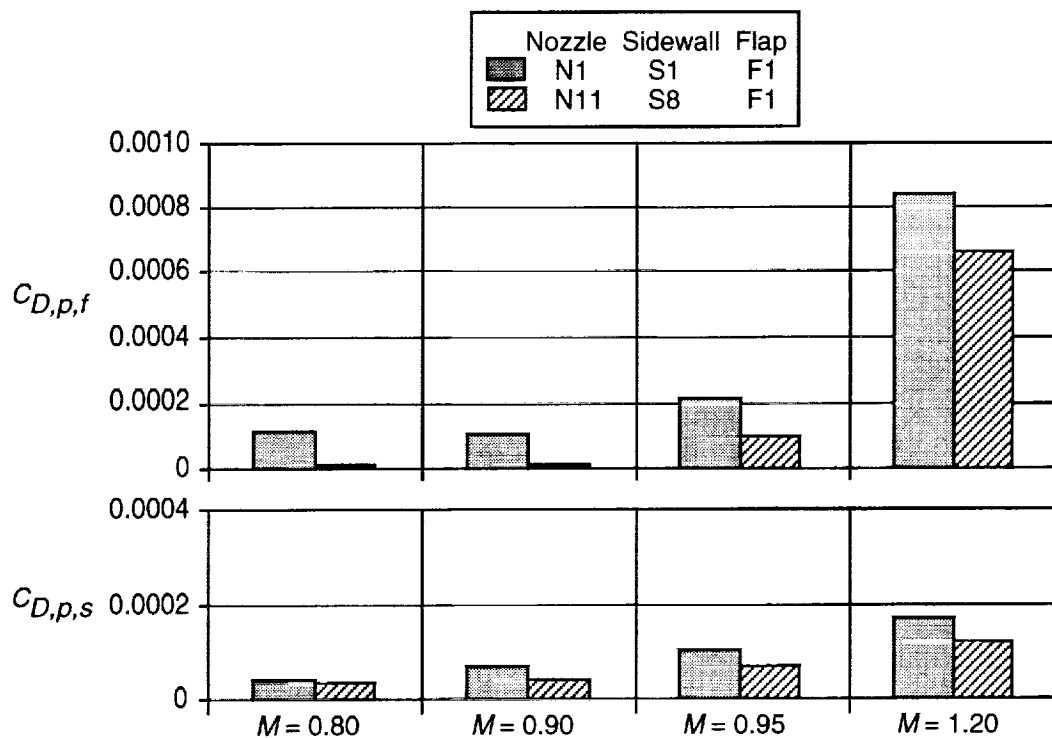


Figure 27. Effect of sidewall height on flap and sidewall pressure drag, NPR = 5.

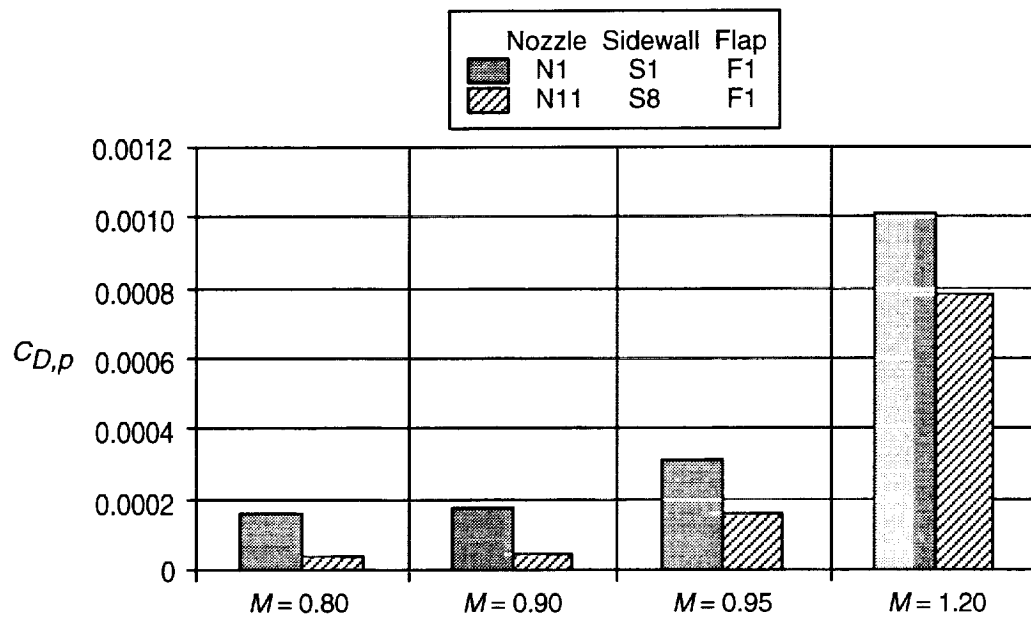


Figure 28. Effect of sidewall height on nozzle pressure drag, NPR = 5.

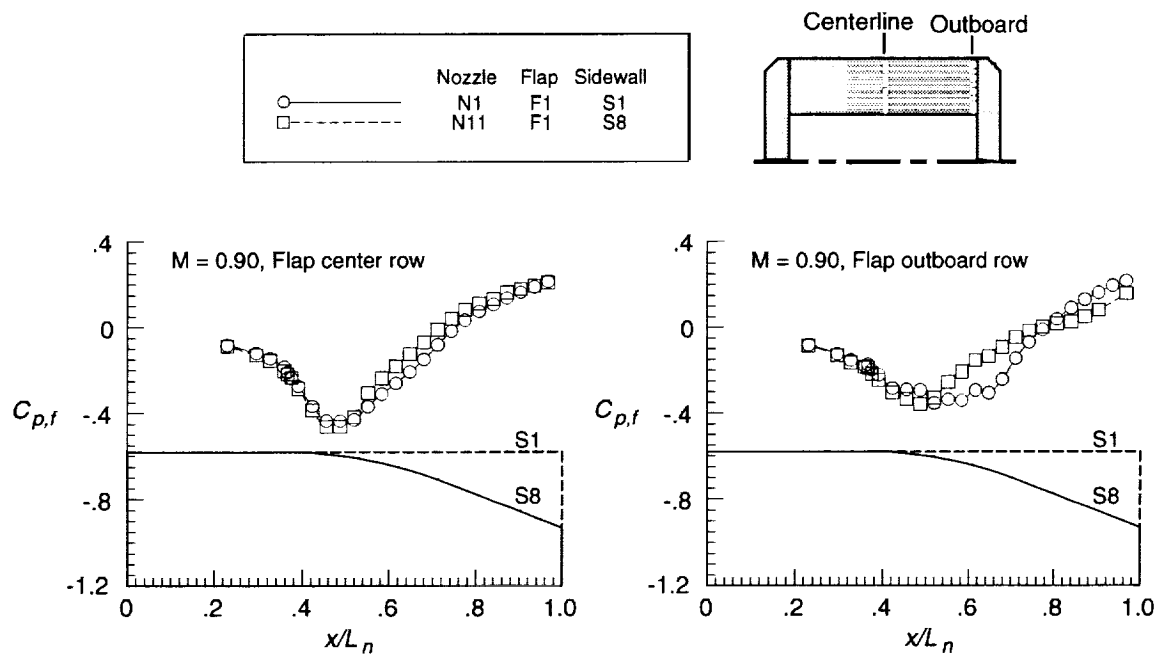


Figure 29. Effect of sidewall height on flap pressure distributions, NPR = 5.

